PCCP

Cite this: *Phys. Chem. Chem. Phys.*, 2012, **14**, 6967–6973

www.rsc.org/pccp

PAPER

Styrene oligomerization as a molecular probe reaction for Brønsted acidity at the nanoscale†

Luis R. Aramburo,[a] Sue Wirick,[b] Piter S. Miedema,[a] Inge L. C. Buurmans,[a] Frank M. F. de Groot[a] and Bert M. Weckhuysen*[a]

Received 7th September 2011, Accepted 19th December 2011
DOI: 10.1039/c2cp22848c

The Brønsted acid-catalyzed oligomerization of 4-fluorostyrene has been studied on a series of H-ZSM-5 zeolite powders, steamed under different conditions, with a combination of UV-Vis micro-spectroscopy and Scanning Transmission X-ray Microscopy (STXM). UV-Vis micro-spectroscopy and STXM have been used to monitor the relative formation of cyclic and linear dimeric carbocations as a function of the steaming post-treatment (*i.e.*, parent *vs.* steaming at 600, 700 and 800 °C). It was found that the UV-Vis band intensity ratios of linear to cyclic dimeric species increase from 0.79 (parent H-ZSM-5) over 1.41 (H-ZSM-5 steamed at 600 °C) and 1.88 (H-ZSM-5 steamed at 700 °C) to 2.33 (H-ZSM-5 steamed at 800 °C). STXM confirms this trend in reaction product selectivity, as the relative intensities of the transitions attributed to the presence of the cyclic dimer in the carbon K-edge spectra decrease with increasing severity of the steaming post-treatment. Furthermore, STXM reveals spatial heterogeneities in reaction product formation within the H-ZSM-5 zeolite powders at the nanoscale. More specifically, a shrinking carbon core–shell distribution was detected within the zeolite aggregates, in which the relative amount of cyclic dimeric species is higher in the core relative to the shell of the zeolite aggregate and the relative amount of cyclic dimeric species in the zeolite core gradually decreases with increasing severity of the steaming post-treatment. These differences are rationalized in terms of spatial differences in Brønsted acidity within H-ZSM-5 zeolite powders as well as by changes in the formation process of linear and dimeric carbocations within H-ZSM-5 micro- and mesopores.

1. Introduction

Zeolite materials have widespread applications as heterogeneous catalysts in the chemical industry due to their acidic and porosity properties.[1–7] Specific framework topologies combined with Brønsted acidity allow the performance of shape selective catalysis, which increases the cost-effectiveness of chemical processes.[8–10] To further boost the catalytic activity and/or selectivity, the properties of zeolites can be adjusted and large efforts have been made to control and hierarchically modify the properties of zeolite materials during their synthesis[11,12] or by using post-treatments.[13–16] Among the latter approaches, dealumination by steaming has become a cheap and efficient way to simultaneously modify the topological and acidic properties of zeolites.[17,18]

To optimize the variation of zeolite characteristics, an in-depth understanding of the physicochemical processes that determine the catalytic properties of zeolite materials is needed. Such information can be obtained in some cases by performing a suitable probe reaction in combination with appropriate spectroscopic methods, such as UV-Vis and (confocal) fluorescence micro-spectroscopy. To achieve this goal, our group has in recent years explored the Brønsted acid catalyzed oligomerization of 4-fluorostyrene as a potential probe for assessing zeolite properties. In this way the macroscopic alignment of the generated reaction products in large ZSM-5 coffin-shaped crystals was used to obtain knowledge about the microscopic topology of its crystal sub-units.[19] Moreover, by making use of IR microscopy it was revealed that the distinct pore alignment of the different sub-units was responsible for the non-uniform catalytic behaviour of the zeolite crystals.[20] In the case of zeolite H-ZSM-5 and H-Y powders, the styrene probe reaction was successfully applied to reveal a relationship between Brønsted acidity and oligomerization activity.[21] However, to visualize possible variations in the catalytic performance of small zeolite aggregates, nanometre scale-resolved spectroscopic methods are required.[22]

In this work, further insight into the experimental factors that influence the Brønsted acid-catalyzed styrene oligomerization

[a] *Inorganic Chemistry and Catalysis, Debye Institute for NanoMaterials Science, Utrecht University, Universiteitsweg 99, 3584 CG Utrecht, The Netherlands. E-mail: b.m.weckhuysen@uu.nl; Fax: +31 (0)30 251 1027*
[b] *Department of Physics and Astronomy, State University of New York at Stony Brook, Stony Brook, NY, USA. E-mail: swirick@bnl.gov; Tel: +1 631-344-5601*

† Electronic supplementary information (ESI) available. See DOI: 10.1039/c2cp22848c

reaction has been obtained by studying a series of zeolite ZSM-5 powders steamed at different temperatures. The zeolite materials have been analyzed with a combination of Scanning Transmission X-ray Microscopy (STXM) and UV-Vis micro-spectroscopy. STXM, combining chemical speciation with nanometre spatial resolution,[23–25] is used to map the different reaction products within the zeolite H-ZSM-5 aggregates, whereas both STXM and UV-Vis micro-spectroscopy provide insight in the changes in reaction product selectivity upon steaming. It will be shown that steaming post-treatment leads to the formation of a shrinking carbon core–shell distribution within the zeolite aggregates. More specifically, the relative amount of cyclic dimeric carbocation species in the centre of the zeolite aggregates decreases at the expense of the formation of linear dimeric carbocation species upon increasing severity of the steaming post-treatment.

2. Experimental

2.1 Catalyst materials and properties

A series of H-ZSM-5 materials differing in their Brønsted acidity was obtained by performing a steaming post-treatment on an industrially relevant ZSM-5 zeolite (CBV2314, Si/Al = 11.5, sample name: H-ZSM-5-P) provided by Zeolyst in its ammonium form. Prior to dealumination, the samples were converted into their protonic form by calcination at 550 °C (2 °C min^{-1}, 180 min) in a quartz tubular oven (Thermoline 79300). Subsequently, the H-ZSM-5 zeolites were steamed during 3 h at 600 °C (sample name: H-ZSM-5-600), 700 °C (sample name: H-ZSM-5-700) and 800 °C (sample name: H-ZSM-5-800) *via* saturation of a N_2 flow (180 ml min^{-1}) with water at 100 °C. After the steaming post-treatment the zeolites were calcined at 550 °C (2 °C min^{-1}, 360 min). N_2 adsorption and desorption isotherms of the zeolite samples were measured at −196 °C on a Micromeritics Tristar 3000 instrument. The corresponding surface areas were calculated using the BET model, whereas the micropore volume was calculated with the t-plot method. These results are summarized in Table 1.

Ammonia temperature programmed desorption (NH_3-TPD) was performed using a Micromeritics AutoChemII 2920 apparatus. The sample, 0.15 g in all cases, was first pretreated in He (25 ml min^{-1}) for 30 min at 600 °C, then cooled down to 100 °C and saturated with ammonia to the equilibrium state. Prior to desorption, samples were flushed in He for 30 min. Subsequently, the ammonia desorption was performed in the range of 100 °C to 600 °C at a heating rate of 10 °C min^{-1}. A reference compound, 4-fluoropolystyrene, was synthesized by heating 30 μl of 4-fluorostyrene (Acros Organic, 97%) at 70 °C for 10 h.

Table 1 Overview of the properties of the H-ZSM-5 materials under investigation, including the type of post-treatment applied, BET surface area and micropore volume of the ZSM-5 materials

	H-ZSM-5-P	H-ZSM-5-600	H-ZSM-5-700	H-ZSM-5-800
Dealumination	No	600	700	800
S BET/m^2 g^{-1}	432	316	315	308
V micro/cm^3 g^{-1}	0.14	0.12	0.12	0.12

2.2 UV-Vis micro-spectroscopy

UV-Vis micro-spectroscopy was performed in an *in situ* cell (FTIR600, Linkam Scientific Instruments) equipped with a temperature controller (Linkam TMS 93). The microscopy set-up used is based on an Olympus BX41 upright microscope with a 50 × 0.5 NA-high (NA: numerical aperture) working distance microscope objective. A 75 W tungsten lamp was used for illumination. The microscope was equipped with a 50/50 double-viewport tube, which accommodated a CCD video camera (ColorView IIIu, Soft Imaging System GmbH) and an optical fibre mount. A 200 mm-core fibre connected the microscope to a CCD UV/Vis spectrometer (AvaSpec-2048TEC, Avantes). Experiments were performed compressing 10 mg of zeolite powder to a pellet and heating it to 120 °C for 5 min, subsequently adding 15 μl of 4-fluorostyrene. After a waiting time of 5 min, UV-Vis spectra were recorded every 5 s with an integration time of 100 ms.

2.3 Scanning transmission X-ray microscopy

The STXM experiments were performed at the X1A beamline of the National Synchrotron Light Source (NSLS) facility at Brookhaven National Laboratory. The monochromized X-ray beam was focused to a spot size of 35 nm using a Fresnel zone plate. The samples were placed on silicon nitride windows, mounted perpendicular to the beam and scanned using a Physik Instruments (Auburn, Ma, USA) piezo nanoposition stage in closed loop mode with a spatial resolution of 5 nm. The carbon K-edge X-ray absorption spectra were obtained by collecting a series of images over small energy increments, subsequently combining these images to form a spectral image sequence (stack). More specifically, the stacks were obtained in the range of 280–310 eV using an energy resolution of 0.1 eV. After spatially aligning the image sequence, principal components analysis (PCA) was used to obtain the primary components in the data set. Another benefit of PCA is that by orthogonalizing the data set the signal/noise ratio increases.[26] Subsequently, a cluster analysis was performed to classify pixels according to similarities in their spectra.[27] The pixel size used in the image sets was 100 × 100 nm.

3. Results and discussion

3.1 UV-Vis micro-spectroscopy

To obtain further insight into the factors that influence the oligomerization of 4-fluorostyrene, the reaction was monitored with UV-Vis micro-spectroscopy. For this purpose, the styrene derivative was added to the parent and steamed H-ZSM-5 zeolite powders, subsequently recording their UV-Vis spectra every 5 s. These spectra are shown in Fig. 1. During the course of reaction different styrene carbocations are formed, which are known to absorb light in the visible region and give rise to strong sample coloration. The distinct species, appearing as a result of the existence of different reaction pathways, are responsible for the alterations in the UV-Vis spectra and a summary of the different reaction pathways is given in Scheme 1. Overall, after the protonation of a styrene monomer (A) by a Brønsted acid site, subsequent addition of another monomer gives rise to the linear dimeric 1,3-bis(4-fluorophenyl)-1-butylium cation (C).

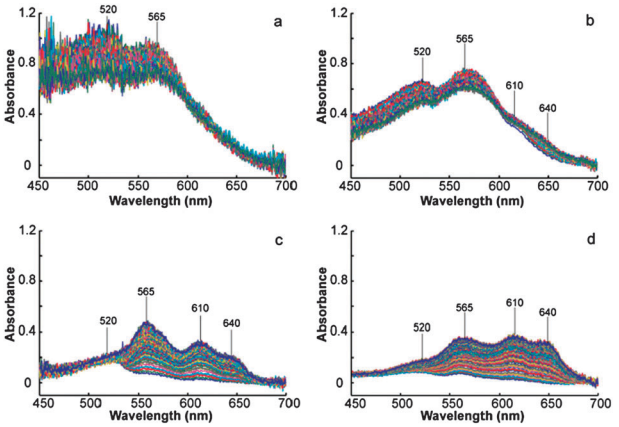

Fig. 1 *In situ* UV-Vis absorption spectra obtained during the Brønsted acid-catalyzed oligomerization of 4-fluorostyrene at 120 °C on H-ZSM-5-P (a), H-ZSM-5-600 (b), H-ZSM-5-700 (c) and H-ZSM-5-800 (d).

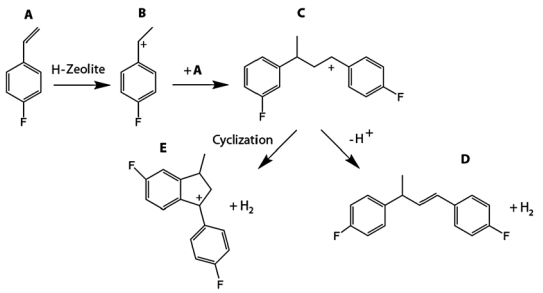

Scheme 1 Competitive reaction pathways in the Brønsted acid-catalyzed oligomerization of 4-fluorostyrene on H-ZSM-5 zeolites. The initial benzylic carbocation (B) is formed due to the protonation of the styrene derivative by a Brønsted acid site. Dimerization with another 4-fluorostyrene monomer (A) gives rise to the linear dimeric 1,3-bis(4-fluorophenyl)-1-butylium cation (C). This carbocation can be transformed either into 3-methyl-1,4-fluorophenylindanyl (E) by a cyclization reaction or into a conjugated linear dimeric 1,3-bis(4-fluorophenyl)-2-buten-1-ylium carbocation (D).

This cation can be further transformed into either a linear dimeric carbocation (D) or a cyclic dimeric carbocation (E). The cyclic dimeric species are characterized by an absorption band at 520 nm, whereas the linear dimeric species are characterized by an absorption band at 565 nm.[21,28]

In Fig. 1(a) the UV-Vis spectra of H-ZSM-5-P show the appearance of absorption bands attributed to both cyclic and linear dimeric carbocations. To quantify the variations in the relative production of both species, the time evolution of both absorption bands has been plotted in Fig. 2 and their relative ratio is presented in Table 2. Closer inspection of the UV-Vis spectra of H-ZSM-5-P reveals a higher intensity of the band located at 520 nm (Fig. 2(b.I)) compared to that present at 565 nm (Fig. 2(a.I)). Analogously, the spectra of H-ZSM-5-600 (Fig. 1(b)) show the appearance of the bands attributed to the cyclic and the linear dimeric carbocations, though the relative intensity of these bands is altered compared to H-ZSM-5-P. Here, the band assigned to the cyclic dimer carbocation has a lower intensity (Fig. 2(b.II)) compared to that of the linear dimer carbocation (Fig. 2(a.II)) leading to a significant variation in the relative ratio of both species. In addition to these bands, new features appear in the

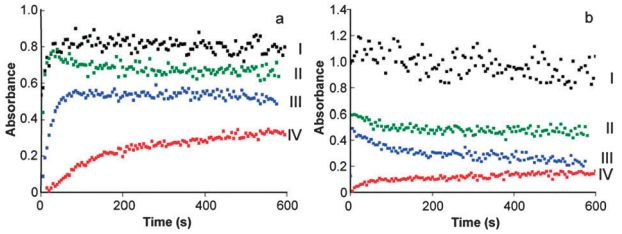

Fig. 2 Time evolution of the intensities of the UV-Vis bands of the linear dimeric carbocation (a) and the cyclic dimeric carbocation (b) for H-ZSM-5-P (I), H-ZSM-5-600 (II), H-ZSM-5-700 (III) and H-ZSM-5-800 (IV).

Table 2 UV-Vis intensities of the bands assigned to the linear dimeric carbocation (565 nm) and to the cyclic dimeric carbocation (520 nm) obtained after 9 min of reaction

Sample	565 nm	520 nm	Linear/cyclic ratio
H-ZSM-5-P	0.81	1.00	0.79
H-ZSM-5-600	0.68	0.48	1.41
H-ZSM-5-700	0.57	0.3	1.88
H-ZSM-5-800	0.21	0.09	2.33

UV-Vis spectra as a result of the steaming post-treatment. More specifically, a band and a shoulder located at 610 nm and 640 nm, assigned to more conjugated linear carbocations.[19,21,28]

When the oligomerization reaction is performed on H-ZSM-5-700, significant differences are observed in the UV-Vis absorption spectra, as shown in Fig. 1(c), where the intensities of the absorption bands at 610 nm and 640 nm drastically increase. This is indicative of a more pronounced formation of linear dimeric carbocations with increasing steaming temperature. In line with this reasoning, the relative intensity of the linear dimer carbocation is enhanced over that of the cyclic dimeric carbocation (Table 2), indicating a variation in the reaction pathways. To further demonstrate the relationship between the changes in the UV-Vis spectra and the steaming pre-treatment conditions, the oligomerization reaction was performed on H-ZSM-5-800. In this case, the UV-Vis spectra show an enhancement in the formation of more conjugated linear oligomers compared to that of H-ZSM-5-700. The absorption bands located at 565, 610 and 640 nm are present in the spectra, while only a small absorption intensity, corresponding to cyclic dimer carbocation formation, is detected. As a result, the values for the ratio of linear dimeric carbocations with respect to cyclic dimeric carbocations are greatly enhanced. Moreover, the relative intensities of the bands assigned to linear carbocations are altered. For H-ZSM-5-600 and H-ZSM-5-700 the relative intensities of the absorption bands follow the same trend (565 nm > 610 nm > 640 nm), whereas for the H-ZSM-5-800 sample the intensities of the absorption bands follow a different tendency (610 nm > 565 nm ≈ 640 nm). These observations indicate an enhanced formation of linear dimeric carbocationic species, as a result of increasing severity of the steaming post-treatment.

In addition, apart from the variations seen in the relative absorption band intensities of the different species, the overall absorption decreases with increasing steaming temperature conditions. This reveals a reduction in the amount of Brønsted acid sites available for reaction. To confirm this observation independent temperature programmed desorption (TPD) experiments with

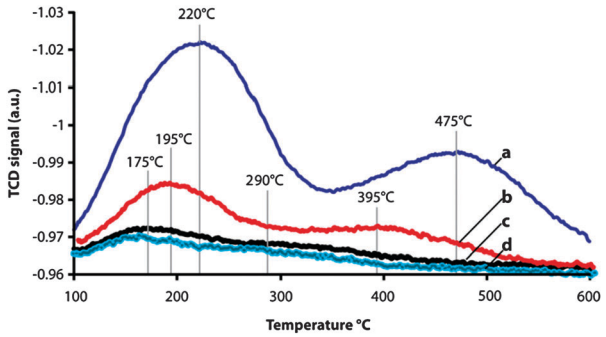

Fig. 3 NH_3-TPD profiles of H-ZSM-5-P (a), H-ZSM-5-600 (b), H-ZSM-5-700 (c) and H-ZSM-5-800 (d).

ammonia as probe molecule have been performed and the results are given in Fig. 3. The NH_3-TPD data clearly reveal a decrease in the overall acidity (*i.e.*, the total area below the curves) with increasing steaming temperature.

3.2 Scanning transmission X-ray microscopy

Soft X-ray micro-spectroscopy of carbon is a useful tool to characterize the distribution and composition of organic matter at the nanometre scale.[24] The promotion of the inner-shell electrons to molecular π* and σ* orbitals is of great utility due to its narrow energy width and chemical sensitivity.[29–31] These transitions give rise to characteristic features in the carbon K-edge X-ray spectra as a result of the chemical bonding of the carbon atoms[32] and render a way to determine possible variations in the product distribution. STXM has been applied in this work to characterize the parent and steamed H-ZSM-5 zeolites by collecting carbon stacks after performing the styrene oligomerization reaction. In a second step, PCA was used to create a covariance matrix from the stack data. The eigenvalues of this matrix result in a set of principal components. Using a sub-set of the covariance matrix, cluster analysis is performed to classify pixels according to similarities in their spectra. In this way, the carbon K-edge X-ray spectra obtained from the most external regions of each H-ZSM-5 sample have been compared in Fig. 4, while the full cluster analysis of the data is presented in Fig. 5.

In Fig. 4 the most prominent transitions present in the carbon K-edge X-ray absorption spectra are shown by comparison of different reference compounds. Among them, the spectral features located at 285 eV and 288.5 eV correspond to transitions from the C 1s to the unoccupied e_{2u} and b_{2g} π* orbitals.[29,33,34] Additionally, the presence of features corresponding to transitions from C 1s to the unoccupied C–H σ*, C–F σ* and C–C σ* molecular orbitals is observed between 287.3–288 eV,[35,36] 290.5–291.5 [37,38] and 290–310 eV,[39] respectively. As depicted in Fig. 4, all reference compounds show transitions to the C–H σ* unoccupied molecular orbital. The small alterations seen in the location of these bands are attributed to energy differences associated with transitions of CH, CH_2 and CH_3 species.[40] The transitions to the unoccupied e_{2u} and b_{2g} π* orbitals are present for benzene, monofluorobenzene and 4-polyfluorostyrene, yet not for perfluoro-2-butene. In contrast, perfluoro-2-butene is the only reference compound that shows a sharp peak attributed to C–F bonds. Logically, this transition is not expected in the spectrum of benzene as a

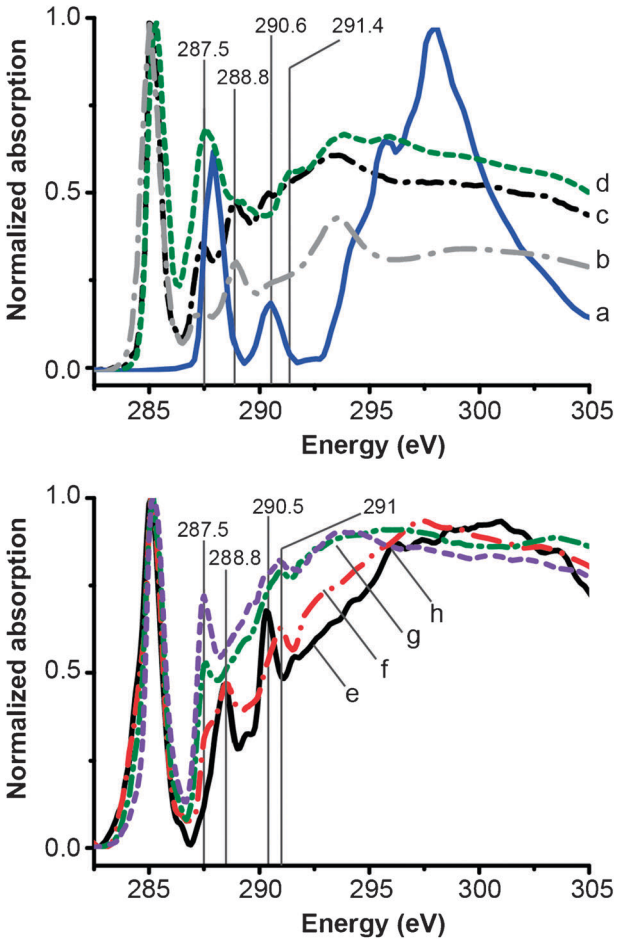

Fig. 4 Carbon K-edge X-ray spectra of perfluoro-2-butene* (a), benzene* (b), 4-fluoropolystyrene (c) and monofluorobenzene* (d). Carbon K-edge X-ray spectra obtained from the cluster analysis performed on H-ZSM-5-P (e), H-ZSM-5-600 (f), H-ZSM-5-700 (g) and H-ZSM-5-800 (h). The spectra marked by * have been digitalized from Hitchcock's group gas phase core excitation data base (http://unicorn.mcmaster.ca/).

result of the lack of C–F bonds. However, one could expect a sharper transition for 4-monofluorobenzene and 4-polyfluorostyrene. In this case, the decrease observed in the intensity of the C–F 1 s → σ* transitions is determined by the alterations in the charge density of the C–F bond. More specifically, in a $C(sp^3)$–F bond, the polarization of the σ bond is partially counterbalanced by redistribution of the electron density, as a result of the conjugation of the 2p atomic orbitals of both atoms. In a $C(sp^2)$–F bond the conjugation of the 2p atomic orbitals is not as effective as in the $C(sp^3)$–F bond, leading to a negligible charge redistribution.[41] Nevertheless, in this type of bond, the excess of charge can be significantly reduced due to the existence of different resonant structures that are able to delocalize the excess of charge.[42] Accordingly, the lower charge density present in the proximity of the $C(sp^2)$–F bond induces a decrease in the C–F σ* transitions. In this way, the differences shown in the carbon XAS of monofluorobenzene and 4-polyfluorostyrene with that of perfluoro-2-butene can be rationalized by a lower excess of charge localized in the proximity of the C–F bond.

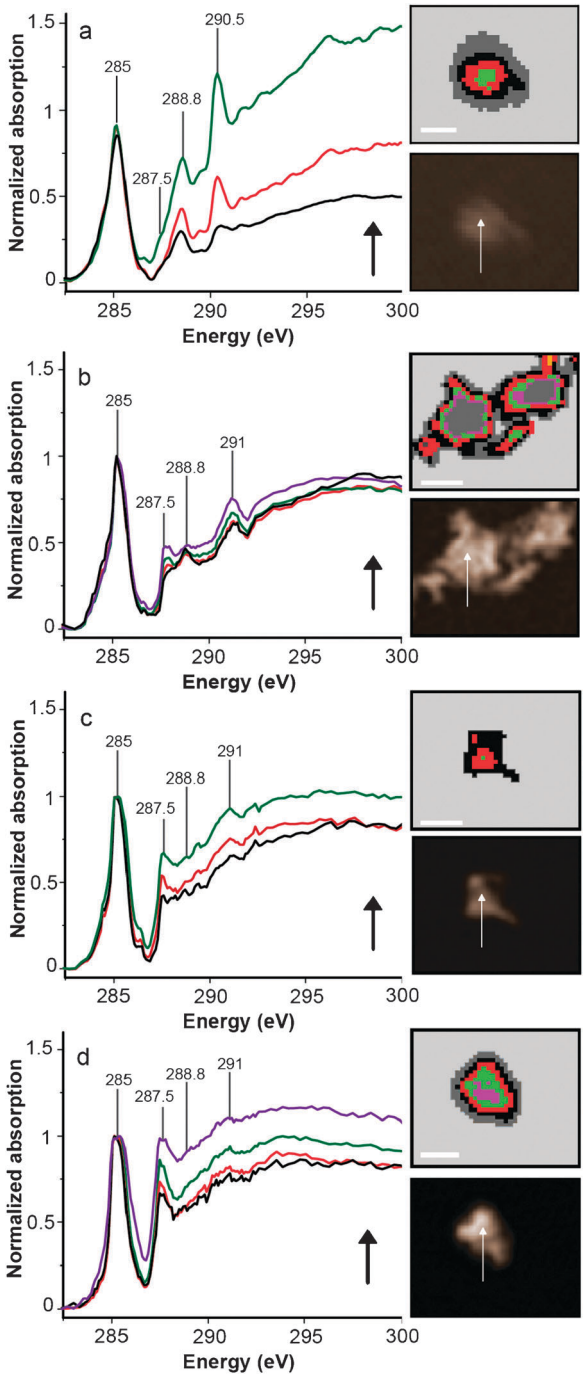

Fig. 5 Left, carbon K-edge X-ray spectra obtained after performing a cluster analysis subsequent to the 4-fluorostyrene oligomerization reaction on H-ZSM-5-P (a), H-ZSM-5-600 (b), H-ZSM-5-700 (c) and H-ZSM-5-800 (d). Right, carbon map and cluster index. The white areas in the cluster index correspond to regions where no signal was collected, whereas the grey areas represent regions that were not used for the analysis. The coloured regions represent the areas from which the spectra (depicted in the left) were collected. The scale bar represents 500 nm in (a) and 1 μm in (b–d).

As a result of the structural differences existing between the cyclic and the linear dimer, STXM can be used to visualize alterations in the relative production of both dimers. More in particular, the variations observed in the transitions to the C–F σ* unoccupied molecular orbital are key to discriminate between both dimers. The lower degree of conjugation of C═C bonds in the cyclic dimer is responsible for the existence of a lower number of resonant structures as compared to the linear dimer. This leads to a lower delocalization of the excess of charge present in the C–F bond, which determines an increase in the transitions to the C–F σ* unoccupied molecular orbital. Consequently, the intensity and position of the feature attributed to C–F σ* transitions has been used in this study as a reporter of the cyclic dimer.

The comparison of the carbon K-edge XAS presented in Fig. 4 reveals substantial differences between H-ZSM-5-P and H-ZSM-5-600, indicating a variation in the catalytic behaviour of both samples. The most significant variation is the decrease shown by the peak located at 290.5 eV in the spectra of H-ZSM-5-P. The reduction seen in this transition can be rationalized by a lower density of charge in the C–F bond. Moreover, the peak shifts towards higher energies in the spectra of H-ZSM-5-600, being located at the same position as for monofluorobenzene and 4-polyfluorostyrene. Consequently, the decrease and shift of this spectral feature in the spectrum of H-ZSM-5-600 constitute an experimental evidence for a decrease in the relative production of cyclic dimer with respect to the linear species. In addition, a decrease in the relative intensity of the peaks located at 285 eV and 287.5 eV (attributed to C═C and C–H bonds, respectively) is observed for H-ZSM-5-600. As an increase in the conjugation of linear oligomers leads to a reduction in the C═C/C–H bond ratio, this variation informs of an enhancement in the selectivity towards more conjugated species after steaming. Both observations are in line with the decrease seen in the UV-Vis band intensity ratios of cyclic to linear dimeric species, as well as with the red shift seen in the UV-Vis spectra of H-ZSM-5-600. The variations seen in the carbon XAS of H-ZSM-5-P and H-ZSM-5-600 are further enhanced once the oligomerization reaction is performed on H-ZSM-5-700. Here, the decrease in the C═C/C–H bond ratio is more significant compared to that of H-ZSM-5-600, indicating a higher selectivity towards the production of more conjugated species. Additionally, the peak attributed to C–F σ* transitions decreases its intensity and is located at the same position as for H-ZSM-5-600. A similar tendency is observed for H-ZSM-5-800, where the differences in the relative intensities of the bands appearing at 285 eV and 287.5 eV are further reduced and the transitions to the C–F σ* unoccupied molecular orbitals are less pronounced. In conclusion, the comparison of the different carbon X-ray spectra provides experimental evidence for a relationship between the reaction pathway and the severity of the steaming conditions.

The question arises if the variations seen in the catalytic behaviour of these samples are related to a heterogeneous product distribution within a single zeolite aggregate. To this end, the spectra obtained from the cluster analysis have been compared, showing important variations between different regions of the zeolite aggregate. Close inspection of the carbon K-edge X-ray spectra obtained for the H-ZSM-5-P sample (Fig. 5(a)) reveals an increase in the peak located at 290.5 eV in the internal regions of the zeolite aggregate, which indicates a higher presence of the cyclic dimeric species.

In addition to the higher production of cyclic dimer species seen in the internal regions of H-ZSM-5-P, a decrease in the C═C/C–H bond ratio is observed comparing the intensities of

the peaks appearing at 285 eV and 287.5 eV, respectively. This is an indication of an enhancement in the selectivity towards more conjugated species in the inner regions of the zeolite aggregate. Similar to H-ZSM-5-P, a decrease in the C═C/C–H bond ratio is observed in the internal clusters of H-ZSM-5-600 (Fig. 5(b)). Nevertheless, in this case the reduction is further enhanced as compared to H-ZSM-5-P. In addition, the spectral feature attributed to C–F σ* transitions shifts its position towards higher energies showing a decrease in its relative intensity in the internal regions of the aggregate. This reveals a more selective production of linear dimeric species inside the zeolite aggregate (at the expense of the cyclic dimeric species) with increasing steaming temperature. In line with this hypothesis, the selectivity towards the production of linear dimeric species is notably enhanced in the H-ZSM-5-700 sample (Fig. 5(c)). Here, the feature associated with the cyclic dimeric species in the carbon X-ray spectra is less evident for the internal regions of the zeolite aggregate, while the C═C/C–H bond ratio is notably reduced. Similar variations were observed for H-ZSM-5-800 (Fig. 5(d)), further confirming the aforementioned tendency.

The alterations shown in the selectivity towards the production of linear species with increasing steaming temperature can be rationalized by a plausible variation in the formation mechanism. Theoretical calculations have demonstrated the existence of two different routes.[43] More specifically, the formation of the linear dimeric species can take place *via* a direct hydride transfer (as presented in Scheme 1) or *via* an interaction between two dimer molecules, as proposed by Corma and García.[28] In a purely microporous ZSM-5 zeolite, the latter mechanism is likely to be suppressed due to the high steric constraints imposed by the framework (despite the computed exothermicity for this route). However, all the samples under study possess a certain degree of mesoporosity, implying a higher driving force for a direct interaction between two dimer molecules. Increasing the steaming temperature conditions leads to a higher development of mesoporosity, consequently enhancing the probability for a direct transfer between two dimer molecules. In addition, it is found that by increasing the severity of the steaming post-treatment the overall Brønsted acidity is reduced, thereby lowering the capability of the catalysts to perform cyclization reactions.[44] More in particular, steamed samples have lost almost all their strong Brønsted acid sites after performing the steaming post-treatment (Fig. 3). In this way, the decrease in the steric constraints imposed by the zeolite material and the loss of strong acid sites are responsible for the observed differences in product selectivity within H-ZSM-5 zeolites.

4. Conclusions

A combination of STXM and UV-Vis micro-spectroscopy has been used to obtain further insights into the 4-fluorostyrene oligomerization reaction as a molecular probe for Brønsted acidity. This has been done by investigating a set of industrially relevant H-ZSM-5 zeolites, which have been steamed under different conditions leading to substantial variations in their Brønsted acidity and porosity properties. Both methods have shown the vast influence of the steaming conditions on the catalytic behaviour of H-ZSM-5 during 4-fluorostyrene oligomerization. UV-Vis micro-spectroscopic measurements have revealed an increase in the selectivity towards the linear dimer carbocations with increasing steaming temperature. STXM further supports these findings as there is an increase in the selectivity towards more conjugated linear species with increasing steaming temperature. Furthermore, the presence of the cyclic dimer species was preferentially observed in the inner regions of the zeolite aggregate. However, its production drastically decreases with increasing severity of the post-treatment. As the formation of the linear and the cyclic dimer species follow different routes, this constitutes a clear indication for a variation in reaction pathways. More specifically, the synchronized variation of the topological and acidic properties with harsher steaming temperature conditions increases the driving force for a bimolecular hydride transfer. Simultaneously, the lower Brønsted acid site strength of the steamed H-ZSM-5 samples reduces the cyclization capability of the zeolite material, suppressing the formation of the cyclic dimer carbocation species. Summarizing, STXM in combination with the styrene oligomerization as a molecular probe reaction allows evaluating Brønsted acidity differences within zeolite materials at the nanoscale.

References

1 G. J. Kramer, R. A. van Santen, C. A. Emeis and A. K. Nowak, *Nature*, 1993, **363**, 529–531.
2 F. Heslot, N. Fraysse and A. M. Cazabat, *Nature*, 1989, **338**, 640–642.
3 J. M. Thomas, *Sci. Am.*, 1992, **266**, 112–118.
4 M. Bejblova, D. Prochazkova and J. Cejka, *ChemSusChem*, 2009, **2**, 486–499.
5 A. Corma, S. B. A. Hamid, S. Iborra and A. Velty, *ChemSusChem*, 2008, **1**, 85–90.
6 V. Calemma, A. Carati, C. Flego, R. Giardino, F. Gagliardi, R. Millini and G. Bellussi, *ChemSusChem*, 2008, **1**, 548–557.
7 B. M. Weckhuysen, *Angew. Chem., Int. Ed.*, 2009, **48**, 4910–4943.
8 C. W. Jones, K. Tsuji and M. E. Davis, *Nature*, 1998, **393**, 52–54.
9 X. C. Wu and R. G. Anthony, *J. Catal.*, 1999, **184**, 294–297.
10 S. M. Csicsery, *Pure Appl. Chem.*, 1986, **58**, 841–856.
11 A. Corma, V. Fornes, S. B. Pergher, T. L. M. Maesen and J. G. Buglass, *Nature*, 1998, **396**, 353–356.
12 A. Corma, V. Fornes, J. Martinez-Triguero and S. B. Pergher, *J. Catal.*, 1999, **186**, 57–63.
13 S. van Donk, A. H. Janssen, J. H. Bitter and K. P. de Jong, *Catal. Rev. Sci. Eng.*, 2003, **45**, 297–319.
14 J. C. Groen, J. A. Moulijn and J. Pérez-Ramírez, *J. Mater. Chem.*, 2006, **16**, 2121–2131.
15 J. C. Groen, W. D. Zhu, S. Brouwer, S. J. Huynink, F. Kapteijn, J. A. Moulijn and J. Pérez-Ramírez, *J. Am. Chem. Soc.*, 2007, **129**, 355–360.
16 L. Jin, H. Hu, S. Zhu and B. Ma, *Catal. Today*, 2010, **149**, 207–211.
17 L. R. Aramburo, L. Karwacki, P. Cubillas, S. Asahina, D. A. M. de Winter, M. R. Drury, I. L. C. Buurmans, E. Stavitski, D. Mores, M. Daturi, P. Bazin, P. Dumas, F. Thibault-Starzyk, J. A. Post, M. W. Anderson, O. Terasaki and B. M. Weckhuysen, *Chem.–Eur. J.*, 2011, **17**, 13773–13778.
18 L. Karwacki, D. A. M. de Winter, L. R. Aramburo, M. N. Lebbinik, M. R. Drury and B. M. Weckhuysen, *Angew. Chem., Int. Ed.*, 2011, **50**, 1294–1298.
19 M. H. F. Kox, E. Stavitski, J. C. Groen, J. Perez-Ramirez, F. Kapteijn and B. M. Weckhuysen, *Chem.–Eur. J.*, 2008, **14**, 1718–1725.
20 M. H. F. Kox, E. Stavitski and B. M. Weckhuysen, *Angew. Chem., Int. Ed.*, 2007, **46**, 3652–3666.
21 I. L. C. Buurmans, E. A. Pidko, J. M. de Groot, E. Stavitski, R. A. van Santen and B. M. Weckhuysen, *Phys. Chem. Chem. Phys.*, 2010, **12**, 7032–7040.

22 A. M. Beale, S. D. M. Jacques and B. M. Weckhuysen, *Chem. Soc. Rev.*, 2010, **39**, 4656–4672.
23 F. M. F. de Groot, E. de Smit, M. M. van Schooneveld, L. R. Aramburo and B. M. Weckhuysen, *ChemPhysChem*, 2010, **11**, 951–962.
24 E. de Smit, I. Swart, J. F. Creemer, G. H. Hoveling, M. K. Gilles, T. Tyliszczak, P. J. Kooyman, H. W. Zandbergen, C. Morin, B. M. Weckhuysen and F. M. F. de Groot, *Nature*, 2008, **456**, 222–226.
25 E. de Smit, I. Swart, J. F. Creemer, C. Karunakaran, D. Bertwistle, H. W. Zandbergen, F. M. F. de Groot and B. M. Weckhuysen, *Angew. Chem., Int. Ed.*, 2009, **48**, 3632–3636.
26 M. Lerotic, C. Jacobsen, T. Schafer and S. Vogt, *Ultramicroscopy*, 2004, **100**, 35–57.
27 M. Lerotic, C. Jacobsen, J. B. Gillow, A. J. Francis, S. Wirick, S. Vogt and J. Maser, *J. Electron Spectrosc. Relat. Phenom.*, 2005, **144**, 1137–1143.
28 A. Corma and H. García, *J. Chem. Soc., Dalton Trans.*, 2000, 138–1139.
29 E. G. Rightor, S. G. Urquhart, A. P. Hitchcock, H. Ade, A. P. Smith, G. E. Mitchell, R. D. Priester, A. Aneja, G. Appel, G. Wilkes and W. E. Lidy, *Macromolecules*, 2002, **35**, 5873–5882.
30 H. Ade, D. A. Winesett, A. P. Smith, S. Anders, T. Stammler, C. Heske, D. Slep, M. H. Rafailovich, J. Sokolov and J. Stöhr, *Appl. Phys. Lett.*, 1998, **73**, 3775–3777.
31 J. A. Brandes, S. Wirick and C. Jacobsen, *J. Synchrotron Radiat.*, 2010, **17**, 676–682.
32 J. A. Horsley, J. Stöhr, A. P. Hitchcock, D. C. Newbury, A. L. Johnson and F. Sette, *J. Chem. Phys.*, 1985, **83**, 6099–6107.
33 H. Ade, X. Zhang, S. Cameron, C. Costello, J. Kirz and S. Williams, *Science*, 1992, **258**, 972–975.
34 P. R. Haberstroh, J. A. Brandes, Y. Gélinas, A. F. Dickens, S. Wirick and G. Cody, *Geochim. Cosmochim. Acta*, 2006, **70**, 1483–1494.
35 D. Solomon, J. Lehman, J. Kinyangi, B. Liang, K. Heymann, L. Dathe and K. Hanley, *Soil Sci. Soc. Am. J.*, 2009, **73**, 1817–1830.
36 A. P. Hitchcock, D. C. Newbury, I. Ishii, J. Stöhr, J. A. Horsley, R. D. Redwing, A. L. Johnson and F. Sette, *J. Chem. Phys.*, 1986, **85**, 4849–4862.
37 A. P. Hitchcock, P. Fischer, A. Gedanken and M. B. Robinson, *J. Phys. Chem.*, 1987, **91**, 535–540.
38 M. L. Gordon, D. Tulumello, G. Cooper, A. P. Hitchcock, P. Glatzel, O. C. Mullins, S. P. Cramer and U. Bergmann, *J. Phys. Chem. A*, 2003, **107**, 8512–8520.
39 A. P. Hitchcock and I. Ishii, *J. Electron Spectrosc. Relat. Phenom.*, 1987, **42**, 11–26.
40 A. P. Hitchcock and D. C. Mancini, *J. Electron Spectrosc. Relat. Phenom.*, 1994, **67**, 1–132.
41 G. G. Furin and G. G. Yakobson, *J. Fluorine Chem.*, 1985, **28**, 241–256.
42 S. Millefiori, A. Millefiori and G. Granozzi, *J. Mol. Struct.*, 1982, **89**, 247–254.
43 E. Stavitski, E. A. Pidko, M. H. F. Kox, E. J. M. Hensen, R. A. van Santen and B. M. Weckhuysen, *Chem.–Eur. J.*, 2010, **16**, 9340–9348.
44 A. Benito, A. Corma, H. García and J. Primo, *Appl. Catal., A*, 1994, **116**, 127–135.